

Modeling acoustic emissions in heterogeneous rocks during tensile fracture with the Discrete Element Method

Published

5th May 2020

<https://doi.org/10.5802/ogeo.5>

Edited by

Cino Viggiani

Université Grenoble Alpes,
Laboratoire 3SR,
Grenoble, France

Reviewed by

Vanessa Magnanimo

MultiScale Mechanics (MSM),
Faculty of Engineering Technology (ET),
MESA+, University of Twente,
The Netherlands

An anonymous reviewer

Giovanni Grasselli

Department of Civil and Mineral
Engineering, University of Toronto,
35 St George St., Toronto, ON M5S 1A4,
Canada

Correspondence

Robert A. Caulk

Univ. Grenoble Alpes, CNRS, Grenoble
INP, 3SR, 38000 Grenoble, France

robert.caulk@3sr-grenoble.fr

rob.caulk@gmail.com

Robert A. Caulk^a

^a Univ. Grenoble Alpes, CNRS, Grenoble INP, 3SR, 38000 Grenoble, France.

Abstract. A computationally efficient and open sourced methodology designed for the investigation of rock matrix heterogeneities and their effect on pre- and post- fracture Acoustic Emission (AE) distributions is presented. First, an image analysis method is proposed for building a statistical model representing rock heterogeneity. The statistical model is generalized and implemented into a discrete element contact model where it efficiently simulates the presence of defects and locally tough regions. The coupling of the heterogeneity model, discrete element model, and acoustic emission model is demonstrated using a numerical three point bending test. The shape parameter of the statistical model, which controls heterogeneity magnitude, is found to control the spatial width of the acoustic emission distribution generated during failure. The same acoustic emission distribution trend is observed in literature for rocks containing various magnitudes of heterogeneity. Further analysis of the numerical AE activity reveals that larger AE events are located directly along the fracture and they are linearly related to their number of constituent interactions. As such, an AE interaction count threshold is identified to distinguish between fracture and damage AE activity. These results demonstrate the ability of the presented methodology to investigate the location and energy release associated with large fracture events for various levels of heterogeneity.

Keywords. Discrete Element Method; rock heterogeneity modeling; acoustic emission; tensile fracture; intrinsic process zone



This article is licensed under the Creative Commons Attribution NonCommercial ShareAlike 4.0 License.



Open Geomechanics is member of the
Centre Mersenne for Open Scientific Publishing

1. Introduction

Rock fracture modeling remains challenging due to complex micromechanical processes such as the interactions of randomly oriented micro-defects, microcrack coalescence, and stochastically distributed grain-grain cementation. These micromechanical processes concentrate stress and localize strain, which result in non-linear stress-strain behaviors, large deformations, and discontinuities. Such behaviors are difficult to model, but numerous studies demonstrate the DEM-Bonded Particle Model's [Potyondy and Cundall, 2004] ability to model emergent non-linear stress-strain behaviors at variable confining pressures [Scholtès and Donzé, 2012b, Wang and Li, 2014]. Although compressive failure is well-modeled in DEM [Hazzard and Young, 2004], tensile failure models lack the experimentally observed acoustic emissions (AE) (micro failures) in the intrinsic process zone (IPZ) [Labuz et al., 1987, Lockner et al., 1992, Zietlow and Labuz, 1998] despite capturing the macroscopic fracture [Mahabadi et al., 2009]. This paper aims to demonstrate the necessity and validity of a physically constructed rock heterogeneity model for accurate simulation of AE activity during tensile rock failure in DEM.

The study of rock heterogeneity modeling can be split into two general groups. Many studies use statistical distributions to vary material parameters, while others model some representative elementary volume of defects directly and upscale behaviors (known as homogenization). Both methods simplify the computationally intractable problem of modeling all imperfections and grain contacts within a rock specimen with the hopes of modeling the macro effect of heterogeneities: non-linear macroscopic behaviors and fracture nucleation. DEM modelers fall into the first group; they generally represent heterogeneities by stochastically assigning micro-properties (interaction stiffness or strength properties) according to macro-property distributions [Potyondy and Cundall, 2004]. Some DEM studies simply use trial and error calibration techniques to determine strength distribution mean and variation parameters [Khazaei et al., 2015, Ma and Huang, 2017]. Continuum methods, such as the Finite Element Method, approach the problem similarly by stochastically controlling the stiffness parameter, failure criteria, or fracture energy [Cai and Kaiser, 2004, Iturrioz et al., 2019, Tang and Kaiser, 1998, Yang et al., 2004]. Liu et al. [2004] investigated and compared a statistical approach to a direct homogenization approach. In the homogenization case, Liu et al. [2004] used microstructure image analysis to build representative elementary volume material properties and geometries deterministically. In the statistical case, Liu et al. [2004] used a Weibull distribution to assign Finite Element strength and elastic properties. It is important to note that the Weibull distribution was characterized by a “homogeneous index”, which was determined based on experimental macroscopic strength and modulus distributions. Liu et al. [2004] concluded that the statistical method closely approximated the deterministic microstructural representative elementary volume method. Garboczi and Day [1995] modeled heterogeneities directly by generating model geometry based on microstructure

imagery. Rabczuk and Eibl [2006] used a damage evolution model to account for heterogeneities within a meshfree concrete fracture model. Ostoja-Starzewski et al. [1994] and Buxton et al. [2001] modeled heterogeneities directly in a lattice spring model by varying spring stiffnesses depending on the solid phase that they appear in, similar to Liu et al. [2004]'s representative elementary volume method. Sfantos and Aliabadi [2007] imposed heterogeneity by randomly orienting anisotropic grains in a multiscale micromechanical boundary element model. Saksala [2015] modeled minerals directly with randomly oriented discontinuities to account for microcracks. In all aforementioned cases, heterogeneity is introduced into models by varying material parameters according to macroscopic material property distributions or modeling the microstructure directly and homogenizing the behavior at larger scales. In comparison, the grain edge-interaction-length-distribution (EILD) presented in this paper is constructed physically by microstructure image analysis. The physically founded EILD is hypothesized to follow the same distribution of grain contact strengths, and is therefore used to stochastically control the particle interaction strengths in an augmented DEM model.

The discrepancies observed between experimental and numerical AE activity for tensile fractures indicate a gap in the micromechanical understanding of how heterogeneities affect rock behavior. Further, the well documented use of macroscopic property distributions to inform microscopic processes suggests a physically founded micromechanical method still needs to be developed for heterogeneity modeling. This study postulates that the missing piece of the traditional DEM-Bonded Particle Model is the lack of physically founded micromechanical material property distributions. Therefore, this paper presents an augmentation of DEM-Bonded Particle Model by stochastically controlling particle interaction properties according to image observations of rock grain interaction lengths. From here on, the distribution of these grain interaction lengths is called an edge-interaction-length-distribution (EILD). It is hypothesized that the EILD represents the rock heterogeneity, which ultimately controls the dimensions of the intrinsic process zone during tensile fracture. The paper presents the method for building and implementing the EILD for use with traditional DEM. In brief, an image analysis measures edge lengths to build a statistical model which is used to factor each DEM bond strength. This combination of image analysis and statistical modeling enables the EILD-augmented DEM model to accommodate naturally occurring stress concentrations as short edge (low strength, existing defects [Zietlow and Labuz, 1998]) interactions break, and long edge (locally tough regions [Alava et al., 2006]) interactions arrest and deflect fracture propagation. Several objectives are met in support of the aforementioned hypothesis. First, the paper outlines the image analysis and EILD parameter estimation. Next, the heterogeneity model is implemented into DEM, where the intrinsic process zone is numerically simulated for a three point bending test. Finally, literature based experimental spatial and load-based intrinsic process zone AE observations are compared to numerical AE data to demonstrate the effect of the EILD in DEM. Ultimately,

the hypothesis is supported by a method that models the mechanical behavior of a heterogeneous rock while maintaining the computationally tractable spatial discretization of uniform particle distributions. After model validation, the study explores the effect of heterogeneity on AE magnitudes and location. Finally, the paper exploits the augmented model to distinguish fracture and damage AE activity for various heterogeneity magnitudes.

The material presented within is closely related to a pre-published and non-peer reviewed technical note which was made available to accelerate user access to the methods and underlying algorithms presented here [Caulk, 2018]. In comparison, the present paper has an improved presentation of methods and results, clarified versions of figures, new figures, a new analysis of elastic wave propagation (Appendix 6.2), and supplementary test scripts.

2. Background

2.1. Acoustic emissions in the Intrinsic Process Zone

Acoustic Emissions are non-destructive observations of brittle material energy release prior, during, and after material fracture. Many researchers correlate AE counts to inelastic strain rates in rocks prior to failure [Boyce et al., 1981, Lockner et al., 1992]. Other studies localize AE to demonstrate clustering, quantify material damage, and elucidate hysteresis [Berkovits and Fang, 1995, Godin et al., 2004, Iturrioz et al., 2019, Meng et al., 2016, Shah and Labuz, 1995, Sondergeld and Estey, 1981], and some even use AE to identify field scale fracture zones [Soma et al., 2002]. AE locations and magnitudes have shed light on heterogeneity controlled rock failures [Lei et al., 2004]. A common observation of all studies is the cloud of AE activity prior to failure, followed by a coalescence of AE at the fracture location [Yang et al., 2012, Zang et al., 1998].

The collection of AE events in modern laboratories depends on computer based detection, signal conversion, and localization [Labuz et al., 2001, Lockner, 1993]. An array of piezoelectric transducers generate voltage changes that are usually sampled with frequency ranges of 100 Hz - 1 MHz. These voltage changes are time stamped and converted to displacements, which can be either inverted [Eitzen and Wadley, 1984, Shah and Labuz, 1995] or plugged into empirical relationships [McLaskey et al., 2015] to determine stress drops and event magnitudes. Additionally, the hypocenter of each event is determined by minimizing residuals of P-Wave arrival times [Lockner et al., 1992, Shearer, 2009, Zang et al., 1998]. In most cases AE activity within the transducer array are accurately localized within 2 mm, but AE hypocenters beyond the array may be inaccurate up to 20 or 30 mm [Zietlow and Labuz, 1998].

The intrinsic process zone (IPZ) is an important region of AE activity defined as a damaged volume of microcracks surrounding a macrocrack at peak load. Originally, the IPZ was observed using AE by Shah and Labuz [1995] and further validated by Zietlow and Labuz [1998] and Labuz

et al. [2001]. Development of the IPZ is attributed to the inherent heterogeneities of geomaterials such as pre-existing microcracks, misshapen grains, and mineral imperfections [Lei et al., 2000]. Each heterogeneity acts to concentrate stress and extend microcracks, yielding a release of elastic waves (Acoustic Emissions). Zietlow and Labuz [1998] used AE locations pre- and post-peak load to show that the IPZ shape and size is a measurable material property similar to the fracture process zone.

Few studies model the IPZ directly. Fakhimi et al. [2002] compared experimental AE to 2D DEM modeled AE for a biaxial test. Comparisons show that the 2D DEM model microcrack cloud thickness was similar to the experimentally observed AE cloud. Another study by Wang et al. [2012] used finite elements to investigate the development of the fracture process zone around a circular opening in rock. Heterogeneity was addressed with a “homogeneous index” [Chun’an Tang, 1997], and acoustic emissions were simulated by recording the released energy of finite elements. Wang et al. [2012] observed an increase of AE cloud width with increasing heterogeneity (decreasing homogeneous index) and determined a qualitative agreement with experimental observations.

DEM lends itself well to the simulation of AE activity since broken bonds are analogous to microcracks. Hazzard and Young [2000] and Hazzard and Young [2002] introduced methods for modeling AE within PFC DEM software [Itasca, 2015]. Many studies extended and validated the methodology by comparing numerical and experimental Gutenberg-Richter b-values, refining energy calculations, and generating synthetic seismograms [Birck et al., 2018, Hazzard and Damjanac, 2013, Khazaei et al., 2015, 2016, Lisjak et al., 2013, Zhang et al., 2017]. In all cases, compressive tests yield clouds of simulated AE that compare well to experimental AE observations. Meanwhile, contrary to experimental observations, numerical simulation of the Brazilian test generally produce clean fractures with very few (if any) broken bonds in regions surrounding the fracture [Cai and Kaiser, 2004, Ma and Huang, 2017, Mahabadi et al., 2009]. These “clean” fractures may match macroscopic ruptures, but the release of energy associated with acoustic emissions observed in experimental Brazilian tests [Rodríguez et al., 2016] is not resolved. In the cases where heterogeneity is considered, the DEM interaction stiffnesses are stochastically distributed according to macroscopic material property distributions. Since it is not computationally tractable to model each grain and defect individually, DEM’s traditional discretization of space needs to be augmented to accommodate for the development of the IPZ.

2.2. Discrete Element Method

The present study uses a spherical Discrete Element Method (DEM) to treat particulate material as an assembly of various sized spheres, each characterized by density and stiffness. Spherical particle interactions and movements are governed by Newton’s second law of motion, which enables the explicit integration of sphere positions through time to determine forces:

$$m_i \ddot{\mathbf{x}}_i = \mathbf{f}_i \quad (1)$$

where m_i is the mass of particle i , $\ddot{\mathbf{x}}_i$ is the acceleration, and \mathbf{f}_i is the traction on the particle which depends on the constitutive law governing particle interactions. For cohesive assemblies, such as rock, the Bonded Particle Model model presented herein treats particle interactions as springs with normal and shear stiffnesses [Scholtès and Donzé, 2012b]. Following a spring description, Hooke's law is used to determine the forces

$$\mathbf{f}_{ij}^n = k_{ij}^n \Delta D_{ij} \cdot \mathbf{n}_{ij}^n \quad (2)$$

where \mathbf{f}_{ij}^n is the normal force applied to the interacting particles i and j , ΔD_{ij} is the difference between the displacement between interacting particles and a predefined equilibrium distance ($\Delta D = D - D_{eq}$). \mathbf{n}_{ij}^n is the unit vector parallel to the interaction, and the spring normal stiffness, k_{ij}^n , is computed assuming two springs are in serial with lengths equal to the interacting particle radii:

$$k_{ij}^n = \frac{E_i r_i E_j r_j}{E_i r_i + E_j r_j} \quad (3)$$

where E and r are microscopic Young's modulus and radius of particle i or j , respectively. Unlike \mathbf{f}^n , the shear force depends on the orientation of both particles and is therefore updated incrementally:

$$\Delta \mathbf{f}_{ij}^s = k_{ij}^s \Delta u_{ij}^s \cdot \mathbf{n}_{ij}^s \quad (4)$$

$$\mathbf{f}_{ij}^s(t) = \mathbf{f}_{ij}^s(t - \Delta t) + \Delta \mathbf{f}_{ij}^s \quad (5)$$

where Δu_{ij}^s is the tangential displacement between particles, \mathbf{n}_{ij}^s is the unit vector parallel to the tangential displacement, and k^s is simply a fraction of k^n . Although some bonded particle model DEM include bending stiffness, the present study does not.

DEM is well established for modeling cohesive material failure (rock fracture), with studies demonstrating realistic failure planes [Tan et al., 2009], accurate experimental reproductions of toughness tests [Bai et al., 2016], non linear tri-axial stress-strain curves [Scholtès and Donzé, 2012b], and even three point bending tests [Nitka and Tejchman, 2016]. In the present model, the normal bond strength criterion is defined by Scholtès and Donzé [2012a] as:

$$\|\mathbf{f}^n\| \leq -t A_{int} \quad (6)$$

where t is the tensile strength of the bond and $A_{int} = \pi \times \min(r_i, r_j)^2$. The maximum allowable shear force for a given interaction follows a modified Mohr-Coulomb model:

$$\|\mathbf{f}^s\| \leq \|\mathbf{f}^n\| \tan \phi_b + c_b A_{int} \quad (7)$$

where ϕ_b and c_b are calibrated microparameters representing the microscopic friction angle and the cohesion of the interaction, respectively.

Scholtès and Donzé [2012a] also increased the interaction range for DEM bodies to simulate grain interlocking. In the present model, the parameter θ_{int} was increased to

increase the equilibrium distance, D_{eq} . If the distance between two particle centers is less than D_{eq} , they are considered to be interacting:

$$D_{eq} = \theta_{int}(r_i + r_j) \quad (8)$$

It is important to note that θ_{int} should not allow interactions to extend across the diameter of another particle:

$$\theta_{int} < \frac{r_{min} + r_{max}}{r_{max}} \quad (9)$$

3. Methods

3.1. Image analysis for construction of Edge Interaction Length Distribution

The image analysis presented herein aims to demonstrate a) the methodology used for collecting grain contact quantities and b) the validity of using a Weibull model to describe grain contact quantities. To start the presentation of the methodology, a cathodoluminescence image is used to easily distinguish between quartz grains and quartz cement (*i.e.*, detrital vs authigenic quartz) as shown in Fig. 1a [Houseknecht, 1991]. The thresholded grains shown in Fig. 1b are further analyzed with ImageJ for particle centroid location $c(x, y)$, particle perimeter coordinates $\mathbf{p}(x, y)$, and particle Feret diameter D_f [Rasband, 2012]. These grain characteristics are used to detect grain edge interactions as follows:

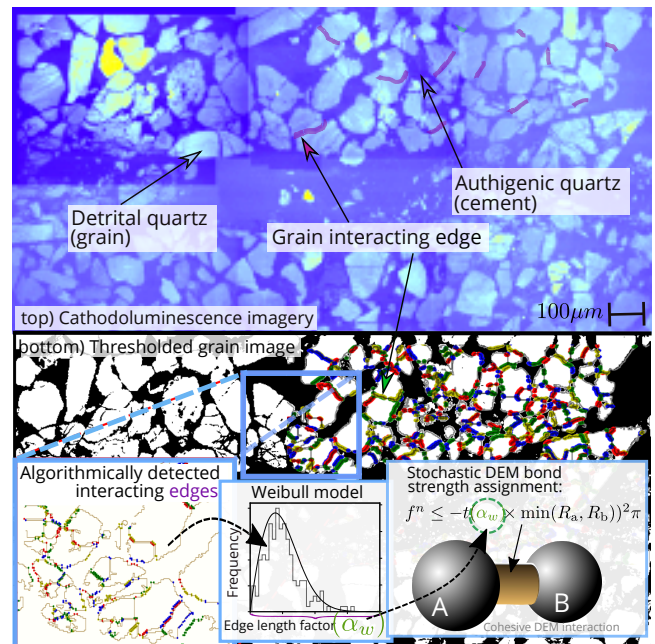


Figure 1. Example of cathodoluminescence imagery used to distinguish between detrital (grains) and authigenic (cement) quartz for image analysis (top). Thresholded detrital quartz (white polygons) and samples of detected interacting edges (colored dots). Example of Weibull model construction and DEM implementation (bottom).

Points of interest on the perimeter of Particle_i ($\mathbf{p}_{i,n}$) are interacting with a single point on the Particle_j ($\mathbf{p}_{j,0}$) if the distance between edge points ($d_{i,n \rightarrow j,0} = \|\mathbf{p}_{i,n} - \mathbf{p}_{j,0}\|$) is less than $D_{i,f}$ multiplied by a separation factor s (selected a priori as 0.2 for this study and is related to the ratio of cement to grains in the specimen):

$$d_{i,n \rightarrow j,0} < sD_{i,f} \quad (10)$$

The process is repeated for all points, n , on the perimeter of Particle_i. The interacting edge length, l_{ij} , between Particle_i and Particle_j is then computed:

$$l_{ij} = \sum_{n=1}^N \|\mathbf{p}_{i,n} - \mathbf{p}_{i,n-1}\| \quad (11)$$

where N is the number of points on Particle_i interacting with Particle_j. A portion of these interacting edges are shown as colored lines between particles in Sub Fig. 1b. As shown in Fig. 2, the final distribution of l follows a Weibull distribution which is parametrically fit using Maximum Likelihood with Newton Raphson (Appendix 6.1). Thus, the grain contact quantities follow a Weibull distribution which is generalized for DEM and parameterized in the remainder of the present study to demonstrate its effect on acoustic emission distributions.

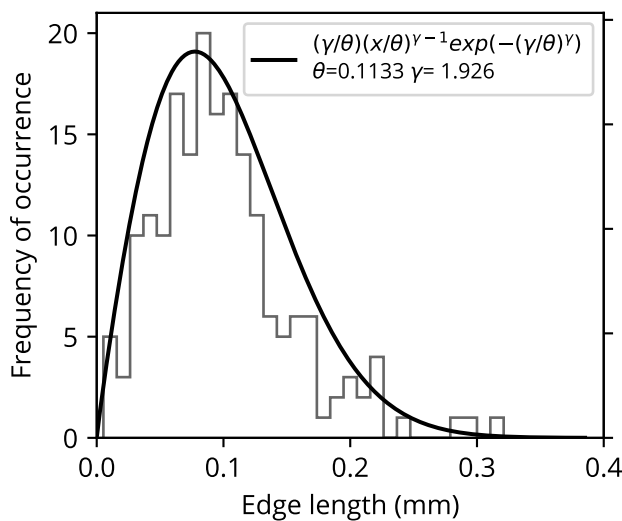


Figure 2. Distribution of interaction edge lengths extracted from Fig. 1

3.2. Implementation of Edge Interaction Length Distribution in DEM

The EILD constructed in Sec. 3.1 represents the distribution of interacting edge lengths between grains in the rock specimen shown in Fig. 1. This paper tests the hypothesis that these interacting edge lengths represent the strength of the grain interactions (*i.e.*, longer interacting edge lengths correspond to higher grain interaction strengths). Such an interpretation can be directly represented in DEM by factoring the radius used to compute the cross-sectional area (A_{int}) in the bond strength calculation (Eq. 6):

$$A_{int} = (\alpha_w \times \min(R_a, R_b))^2 \pi \quad (12)$$

where α_w is a random deviate generated from the EILD distribution (examples of various EILDs shown in Fig. 3). Thus, α_w probabilistically weakens or strengthens a bond according to microstructure imagery observations. In this way, α_w introduces natural heterogeneities and grain structure into a uniformly distributed DEM packing. After Eq. 12 and Eq. 6 are applied to each bond, the final bond strength distributions closely follow the distribution of the random deviate squared, as expected (Fig. 4).

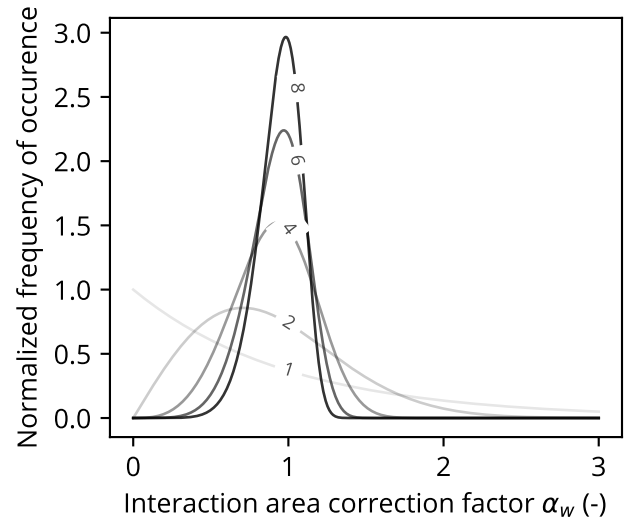


Figure 3. Weibull distributions of α_w for varying magnitude of the Weibull shape parameters.

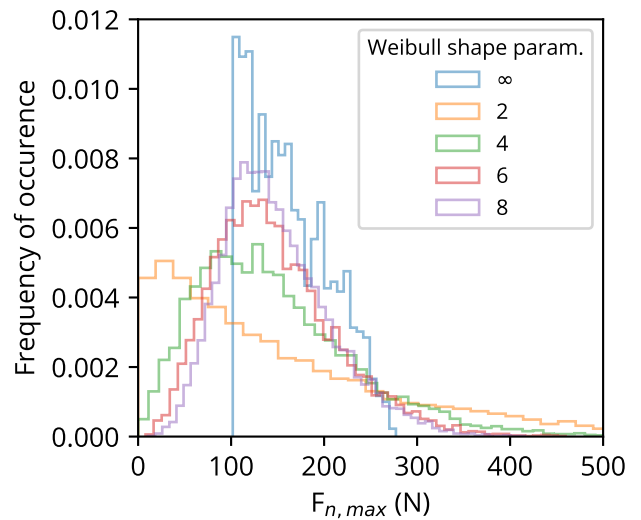


Figure 4. Maximum DEM particle bond tensile strength distributions for varying Weibull shape parameters, γ . Smaller γ correspond to greater heterogeneity.

3.3. Acoustic Emission model in DEM

The current study simulates AE by adopting the DEM interaction strain energy methodology presented by Hazzard

and Young [2000] and Hazzard and Damjanac [2013]. Numerically simulated AE events are simulated by assuming each broken DEM bond (or cluster of broken bonds) represents an event location (Fig. 5), while the associated system strain energy change is empirically related to the event magnitude. Once a bond breaks, the strain energies (u_i) are summed for all intact bonds within a predefined radius:

$$u_i = \frac{1}{2} \left(\frac{f_n^2}{k_n} + \frac{f_s^2}{k_s} \right) \quad (13)$$

$$U_o = \sum_{i=1}^n u_i \quad (14)$$

where U_o is the reference strain energy, n is the number of interactions within the particle neighborhood, f_n , f_s and k_n , k_s are the normal and shear force and stiffness components of the interaction prior to failure, respectively. Hazzard and Damjanac [2013] showed that a volume constrained by 2 to 5 particle diameters (λ) captured the strain energy change of the entire system due to the broken bond of interest⁽¹⁾. After the initial break, ΔU is computed for each subsequent time step:

$$\Delta U = U_o - \sum_{i=1}^n u_i \quad (15)$$

The present implementation defines a time step window (T_{\max}) based on the P-Wave velocity associated with interacting particle densities [Khazaei et al., 2016]:

$$T_{\max} = \text{int} \left(\frac{D_{\text{avg}} \lambda}{\max(v_{p1}, v_{p1}) \Delta t} \right) \quad (16)$$

where D_{avg} is the average diameter of the particles comprising the failed event (m), the P-Wave velocity depends on the interacting particle densities and moduli ($v_p = \sqrt{E/\rho}$ m/s), and Δt is the time step of the simulation (seconds/time step). Finally, $\max(\Delta U)$ obtained during the time step window is used in the empirical equation derived by Scholz and Harris [2003] to compute the moment magnitude of the acoustic event.

$$M_e = \frac{2}{3} \log \Delta U - 3.2 \quad (17)$$

Since AE waveforms are naturally generated by clusters of microcracks [Lockner, 1993, Scholz and Harris, 2003], broken DEM bonds are also clustered. Events are clustered if they occur within spatial and temporal windows of other events (similar to the approach presented by Hazzard and Young [2000], Hazzard and Damjanac [2013]). The final location of a clustered event is simply the average of the clustered event centroids. Here, the updated reference strain energy is computed by adding the strain energy of the unique interactions surrounding the new broken bond to the original reference strain energy (U_o):

- Original bond breaks, sum strain energy of broken bonds (n_{orig}) within spatial window

$$U_{\text{orig},o} = \sum_{i=1}^{n_{\text{orig}}} u_i \quad (18)$$

⁽¹⁾Beyond 2-5 particle diameters, the strain energy change contribution is so small that it is not worth the computational effort necessary to obtain it.

- New broken bond detected within spatial and temporal window of original bond break
- Update reference strain energy, U_o , by adding unique bonds (n_{new}) within new broken bond spatial window

$$U_{\text{new},o} = U_{\text{orig},o} + \sum_{i=1}^{n_{\text{new}}} u_i \quad (19)$$

This particular clustering method maintains a physical reference strain energy for the calculation of $\Delta U = U_{\text{new},o} - \sum_{i=1}^n u_i$. This method will only work for spatial windows at the scale of multiple particle diameters. Since Hazzard and Damjanac [2013] demonstrated that 2-5 particle diameters captures the strain energy change of the entire specimen, the window should not be extended beyond this range. Ultimately, the clustering increases the number of larger events, which yields more comparable b-values of the Gutenberg Richter curve [Hazzard and Damjanac, 2013].

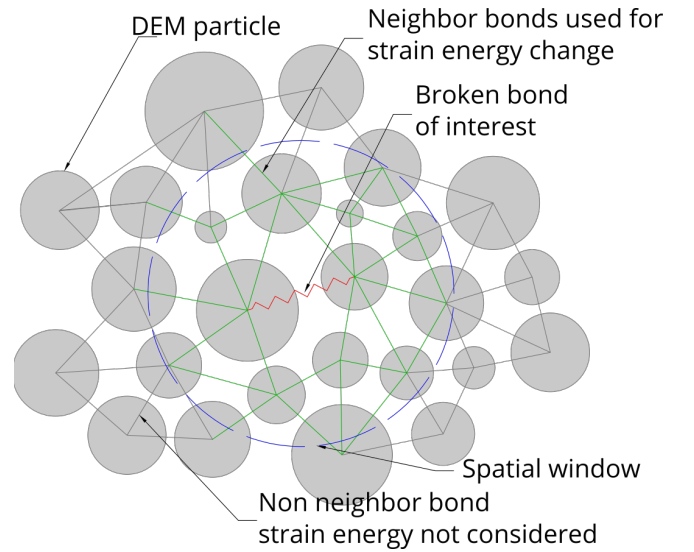


Figure 5. Neighborhood surrounding initial broken bond used for strain energy change estimate in DEM

Additional evidence for the physical accuracy of this DEM AE model can be found in Appendix 6.2. There, the author uses numerical elastic wave arrival times to localize numerical AE events. The similarity of the AE event locations estimated by arrival time inversion and the AE method presented here shows that the elastic waves are behaving similarly to those observed experimentally.

3.4. Three point bending test and DEM model descriptions

The current study explores the effect of the DEM heterogeneity model (Sec. 3.1 and 3.2) on numerical AE (Sec.3.3) during a common three point bending test. Generally, the three point bending test is used to measure the tensile strength and the mode I fracture toughness (K_{Ic}) of a material. In addition to these material characterizations, Zietlow and Labuz [1998] used the three point bending test to experimentally investigate the effect of rock heterogeneity on AE spatial and load based distributions. These experimental

trends are used in this paper to verify numerical AE distribution trends associated with a tensile dominated fracture generated by a three point bending test for increasing levels of numerical heterogeneity. Shear based loading conditions are not explored in this study, but the methods do not prevent such application.

The numerical and experimental setups are identical; specimens measure 80 mm x 240 mm x 40 mm, they are both loaded at the top middle, and they are restrained at both ends as shown in Fig. 6. A loading rate of 0.01 m/s was selected to reduce computational cost while maintaining an inertial number below the “critical state” threshold as recommended by Da Cruz et al. [2005] and implemented for a DEM three point bending test in [Nitka and Tejchman, 2016]:

$$I = \dot{\epsilon} \sqrt{\frac{m}{P d_{min}}} < 10^{-3} \quad (20)$$

where $\dot{\epsilon}$ is the loading rate, d_{min} is the minimum particle diameter, m is the particle’s mass, and P is the pressure used to generate the random dense pack before adding cohesion between particles.

The uniform particle size distribution used here was selected to resolve a realistic acoustic emission magnitude distribution (discussed in Sec. 4.2, Fig 8) while coarse enough to reduce computational cost (as discussed in Sec. 1). DEM particle microproperties are highlighted in Table 1 and were loosely calibrated to the deformation and strength of the experimental sandstone in Zietlow and Labuz [1998] by first calibrating deformation microparameters and finally calibrating strength microparameters. However, toward the goal of isolating the effect of the Weibull shape parameter (γ) on IPZ characteristics, a parametric sweep of γ is performed without altering the remaining DEM micro properties. Thus, a perfect calibration of each experimental rock specimen was not performed. Instead, the experimental data presented by Zietlow and Labuz [1998] is used to verify the numerical IPZ trends.

Table 1. DEM rock specimen microproperties

Micro parameter	Value (DEM)
E_i	30 GPa
k_s/k_n	0.30
ϕ_b	19°
c_b	40 MPa
t	9 MPa
θ_{int}	1.329
Sphere radius	unif(1.125 mm, 1.875 mm)
Sphere density	5000 kg/m^3
γ	2, 4, 6, ∞
λ	3 (particle diameters)

3.5. Practical reproduction of results

All aforementioned methods are available in Yade open DEM code [Smilauer et al., 2015]. Installation instructions for the code can be found on the web.⁽²⁾ For reproduction

⁽²⁾<https://yade-dem.org/doc/installation.html>

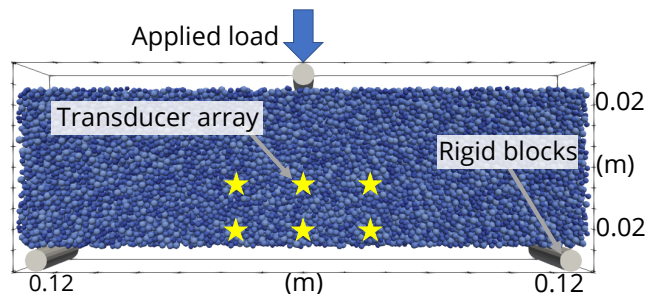


Figure 6. Numerical specimen and three point bending test geometry. Spheres colored by radius (uniform distribution with radius $1.5 \text{ mm} \pm 0.375 \text{ mm}$).

of results, the installed Yade should be used to execute the accompanying python script titled bendingTest.py. Source code for the heterogeneity and acoustic emission models can be found on the web.⁽³⁾ Visualization of acoustic emissions is performed using Paraview [Ahrens et al., 2005].

4. Results and Discussion

Similar to experimental results, the introduction of various levels of “rock heterogeneity” into DEM yields various spatial distributions of acoustic emissions during three point bending tests. This qualitative result is combined with a quantitative validation of AE event magnitudes to perform an analysis of the relationship between event magnitude and geometrical size. These results all combine to enable the distinction between fracture and non-fracture activity in the DEM model.

4.1. Comparison of numerical and experimental three point bending test results

Three point bending test load vs deflection curves show that γ does not have a large impact on stiffness, and strengths are also barely affected with tensile strengths ranging between 7.8-8 MPa in heterogeneous specimens. In comparison to the experimental curve, numerical specimens exhibit less pre-failure plasticity and no “snap-back” behavior (brief reversal of deflection) in comparison to experimental observations (Fig. 7a). These disparities are a result of the contribution to deformation of the experimental machine stiffness leading to a “masked” response (Fig. 7b [Labuz and Biolzi, 2007]). Numerically, the “loading machine” maintains infinite stiffness, and therefore yields a truer response as shown in Fig. 7b. Additional load vs deflection disparities can be attributed to rock specimen differences compared to the generic DEM rock specimen designed to isolate the effect of γ (Sec.3.4).

4.2. Acoustic Emission magnitude distribution in DEM

The AE model described in Sec. 3.3 is validated by magnitude size and distribution. Fig. 8 shows an example of

⁽³⁾<https://gitlab.com/yade-dev/trunk/blob/master/pkg/dem/JoinedCohesiveFrictionalPM.cpp>

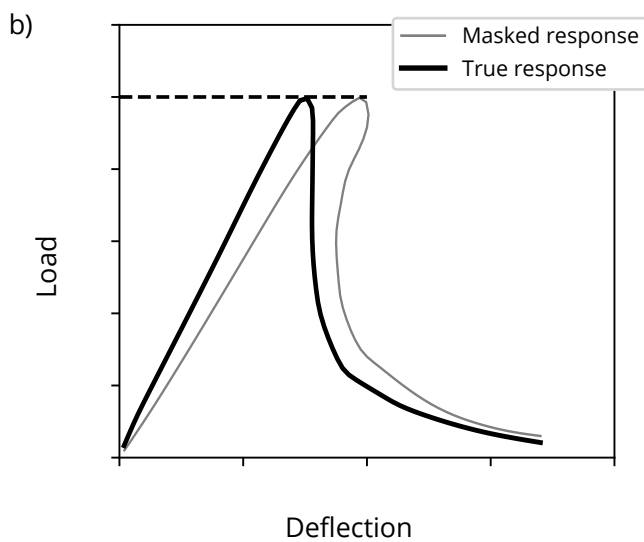
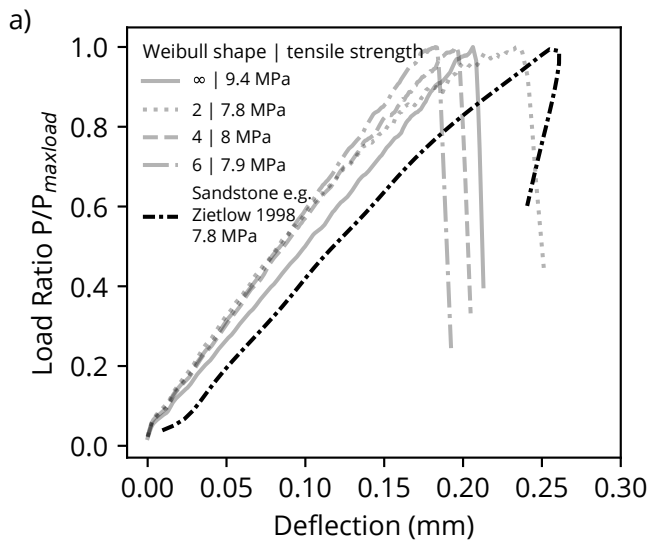


Figure 7. a) Load as a function of deflection for numerical three point bending test for various Weibull shape parameter, γ , values Experimental three point bending test data collected by Zietlow and Labuz [1998]. b) Masked and true failure curves for infinite and finite laboratory loading machine stiffnesses [Labuz and Biolzi, 2007]

the AE magnitude distribution for $\gamma=4$. As shown, the mean event magnitude is -12 and the maximum magnitude is -6.8, which correspond closely to experimentally observed AE magnitudes [Li and Einstein, 2017]. Finally, the distribution exhibits a realistic b-value of 0.84, which is close to the experimentally observed b-value of 1 reported by Rao and Lakshmi [2005] and Scholz [1968].

4.3. Impact of heterogeneity model on Acoustic Emission spatial distribution

Simulated AE follow the spatial and load-based experimental observations presented by Zietlow and Labuz [1998].

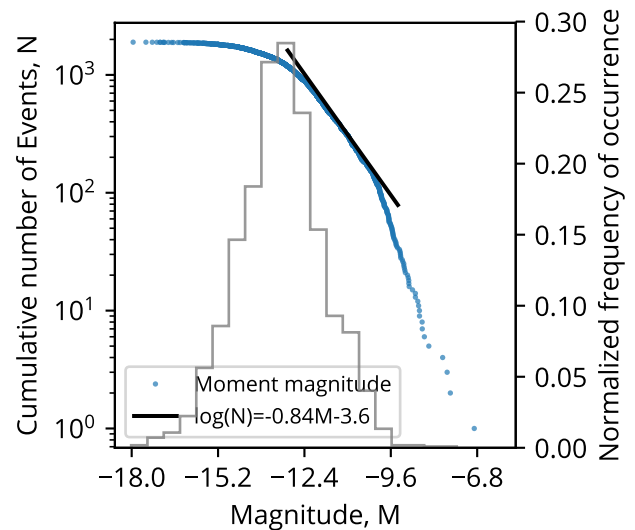


Figure 8. Numerical model AE magnitude distribution (Weibull, shape parameter=4)

Fig. 9 shows how the AE count increases with decreasing γ values (increasing heterogeneity). In DEM the result is interpreted as additional bonds failing as bond strength variation increases. For all γ values, the majority of failure AE occurs between 95 and 100% of the max load. In comparison to the experimental sandstone specimen, numerical specimen AE activity begins at the same load ratio of ca. 70% ($\gamma = 6$). Zietlow and Labuz [1998] also observed an initiation of AE activity around 50% load ratio for a more heterogeneous rock, matching the initiation of AE activity in the $\gamma = 2$ numerical specimen.

Numerically simulated spatial AE distributions also match experimentally observed AE spatial distributions from Zietlow and Labuz [1998]; simulated AE events are distributed randomly during 90-95% max load, followed by a concentration of activity around the fracture after 95% max load (Fig. 10). Numerical AE cloud size characteristics also match experimental observations. A γ value of 2 yields an IPZ width of 30-40 mm, while a $\gamma = \infty$ (traditional model) yields an IPZ width of ≤ 5 mm. The pre-fracture AE cloud narrows as well, with nearly 0 pre-fracture events occurring in the traditional DEM model. In comparison to laboratory results, Zietlow and Labuz [1998] reported that IPZ sizes increased from 5 to 30 mm with rock grain size (Sub Figs. 10), and thus the larger grain size distributions associated with more inherent heterogeneity.

Despite the experimental weakness associated with a loss of AE localization confidence beyond the AE sensor array [Zietlow and Labuz, 1998] both experimental and numerical fractures track through the center of the IPZ AE clouds (Sub Figures 10) with the largest AE events occurring exactly along the macroscopic failure as shown in Fig. 11a. Any disparities between numerical and experimental AE counts/locations are likely caused by the laboratory piezometric transducer threshold limitations, triangulation uncertainties, and unique rock specimen macro behaviors. In particular, the AE collection system described by Zietlow and Labuz [1998] was unable to collect more than 64 events

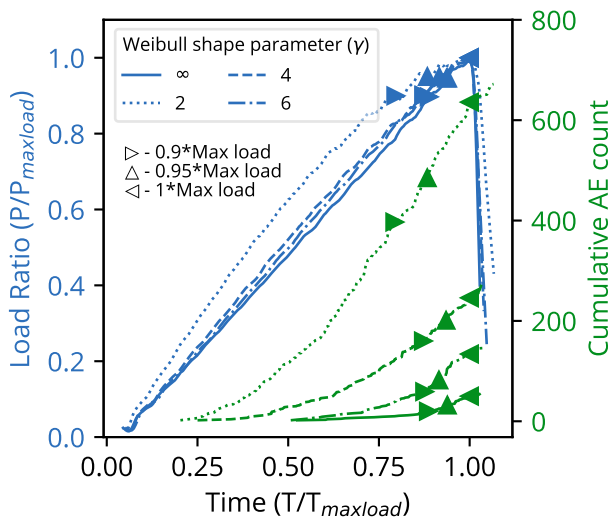


Figure 9. Load and AE count as a function of time for numerical three point bending tests.

simultaneously above a 10 mV threshold. In comparison, the DEM model does not use a threshold and is not limited by the number of events that can be collected simultaneously. Further, many of the behaviorally descriptive DEM microparameters, such as interaction range, bond strengths, and stiffnesses, will also impact the spatial and load-based AE distribution. Therefore, it is important to reiterate that the results presented here demonstrate the influence of the Weibull shape parameter on the spatial and load-based distributions of simulated AE activity in a DEM.

4.4. Characterization of “fracture event” acoustic emission events

The simulated AE magnitudes enable further investigation and distinction of larger AE events, responsible for the tensile fracture, and smaller damage AE events scattered throughout the IPZ. As Sec. 3.3 highlights, each single acoustic emission in the DEM model is comprised of a cluster of broken bonds that occur within a P-Wave scale of space and time. Combined with the estimate of magnitude, the relationship between acoustic emission geometric size and magnitude is analyzed in an attempt to characterize and distinguish “fracture events” from “damage events”.

In the case of moderate heterogeneity, $\gamma=4$, Fig. 11b shows how the largest event (M-6.14) is located at the center of the fracture. AE magnitude decreases as the AE event location moves away from the fracture and into the damaged region of the specimen (Fig. 11a). Figures 12- 14 present a closer look at the large numerical AE events and their clustered interactions (Sec. 3.3). In particular, Fig. 12a) shows how the fracture plane is defined by AE events comprised of more than 10 interactions. Meanwhile, Fig. 12b) plots this relationship and identifies the “fracture event threshold” to distinguish between the large AE focused along the fracture plane and the remaining small damage events scattered throughout the IPZ. The same pattern is observed

by extending the investigation to no-heterogeneity, $\gamma = \infty$ (Fig. 13), and maximum heterogeneity, $\gamma=2$ (Fig.14); a well defined fracture comprised of large AE events, despite the increase of IPZ width.

These results indicate that an increase of heterogeneity corresponds to a more distributed release of energy along the fracture plane. The numerical specimen exhibiting a similar IPZ size as a Charcoal Granite ($k=2$) produced nineteen events comprised of ≥ 10 interactions occurred along the fracture plane (Fig. 14). The largest event registered at M-7.87 and was comprised of 28 interactions. At the other end of the spectrum, the least heterogeneous specimen exhibited a sharper release of energy through fewer events (Fig. 13). Five events comprised of ≥ 10 interactions occurred along the fracture plane for the least heterogeneous specimen. The largest event registered at M-6.49 and was comprised of ca. 400 interactions. Between the two heterogeneity extremes, a numerical specimen exhibiting the same IPZ width as a Sioux Quartzite produced ≥ 10 interactions occurred along the fracture plane (Fig. 12), with the largest event registering at M-6.14 and comprised of ca. 300 interactions. For all specimens, the logarithm of clustered interactions beyond the fracture threshold (≥ 10) is linearly related to their event magnitudes (Fig. 12-14). Below the fracture threshold, the activity follows no distinct pattern and extends beyond the fracture and into the IPZ, and then extends beyond the IPZ and into the pre-failure activity. Thus, for these numerical specimens, the fracture AE activity is easily distinguished from damaged rock AE activity by specifying a threshold of ≥ 10 for the number of constituent interactions. These results indicate that large AE events located along the fracture release more energy from larger rock volumes. This intuitive observation provides insight into the numerical specimen behavior. As Sec. 3.3 describes, the event magnitude depends on the *change* of strain energy in bonds surrounding the event. Further, the interactions are clustered (due to spatial and temporal proximities), by increasing the reference strain energy (Eq. 19). In other words, new bonds actually *decrease* the change of strain energy value and therefore the AE magnitude. It follows that the event magnitude can only increase if a truly large material strain energy change occurs over a several grain spatial scale and a P-Wave velocity time scale. The break down of true heterogeneous rock samples may follow a similar spatial/temporal defect coalescence during the generation of large AE fracture events. Meanwhile, small events located beyond the IPZ may be discounted as non-fracture events, instead they are indicative of a damaged volume within the material. These findings enable the distinction between large fracture events at the center of the IPZ and non-fracture AE activity occurring in the damaged volume surrounding the fracture.

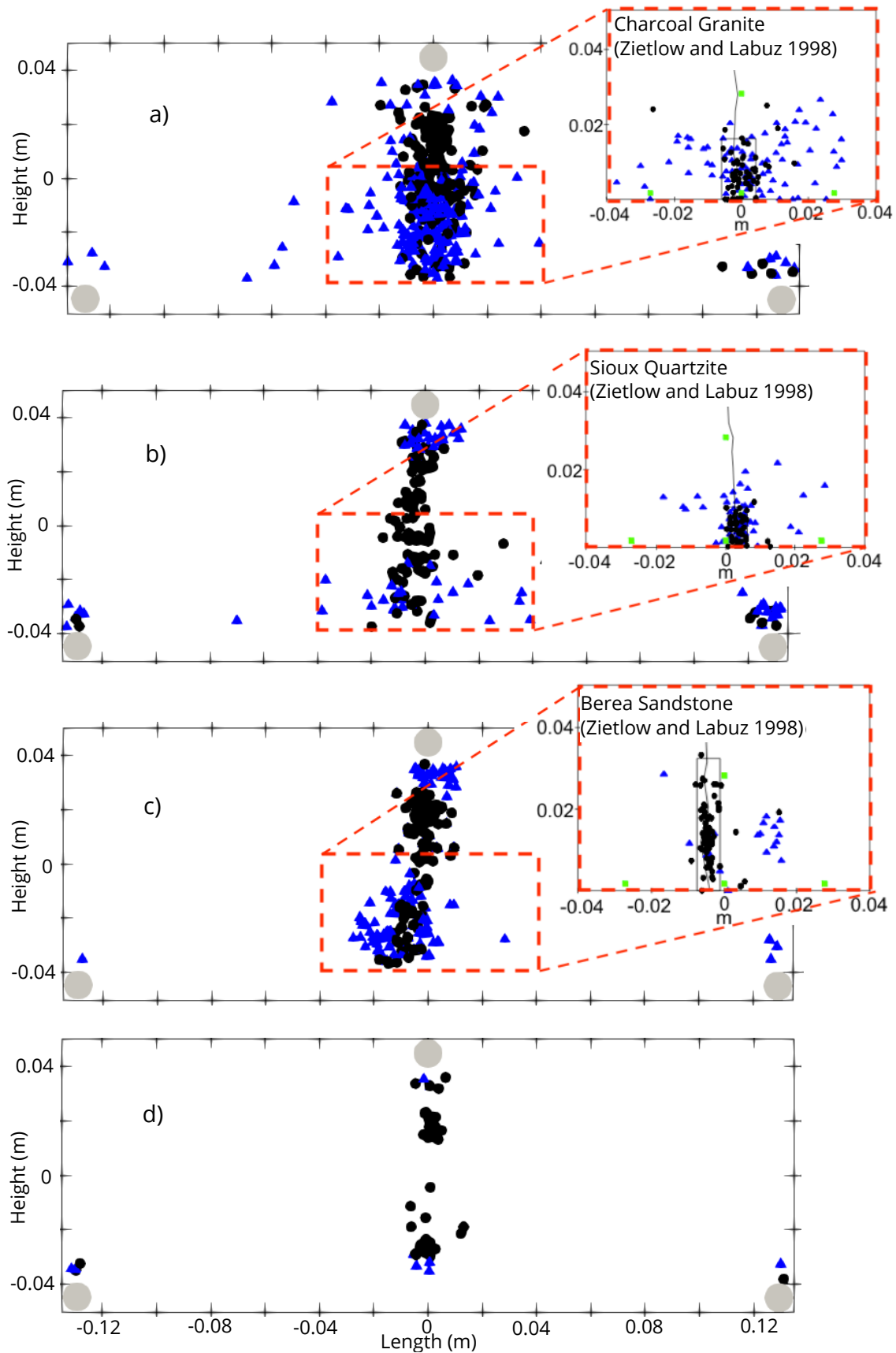


Figure 10. AE distribution for numerical three point bending test (Weibull, shape parameter = a) 2, b) 4, c) 6 d) ∞). Blue triangles represent AE activity between 88-95% max load. Black circles represent AE activity between 95% max load and failure. Comparable experimental results shown as sub-figures [Zietlow and Labuz, 1998]. Green squares within sub-figures represent the transducer array used by Zietlow and Labuz [1998].

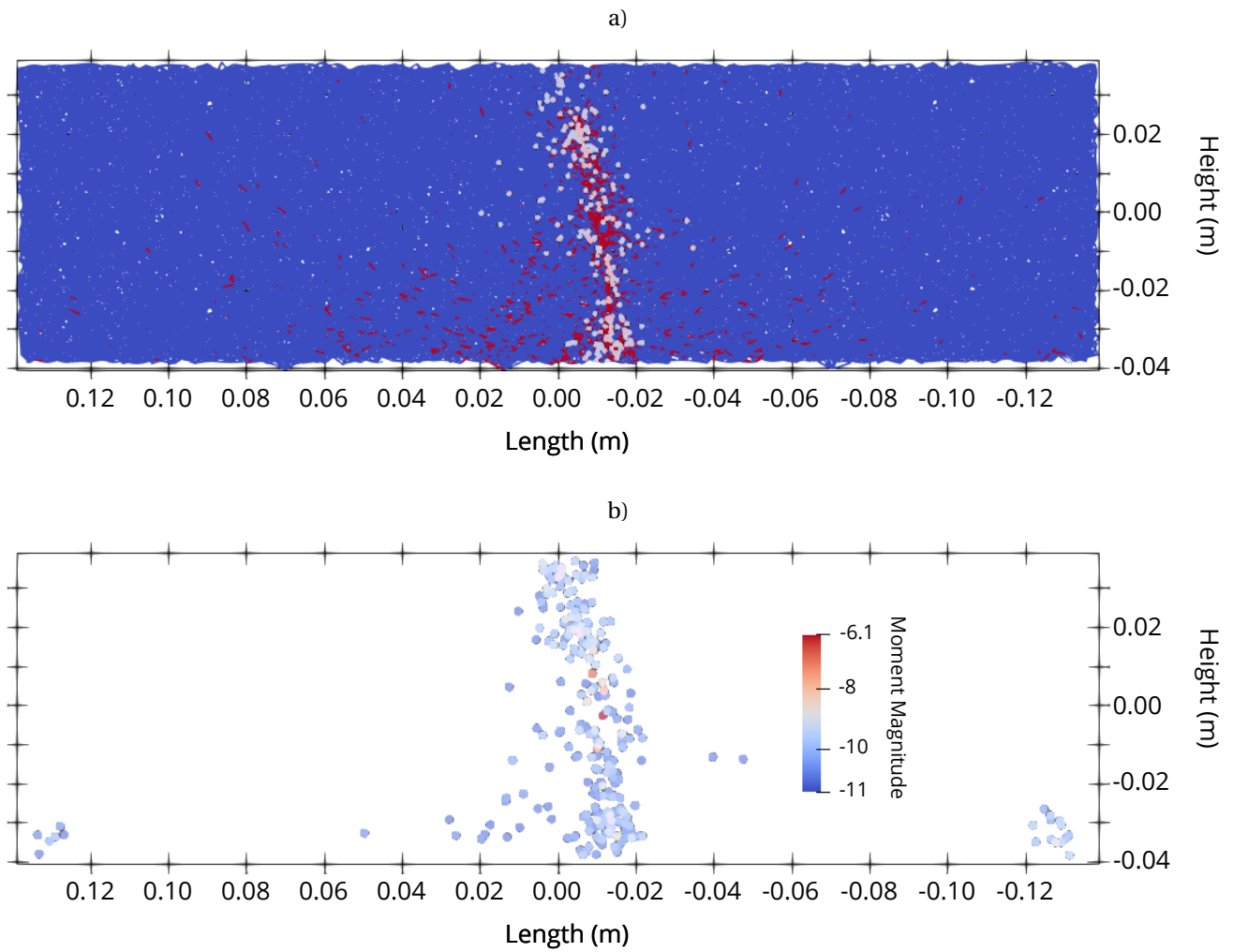
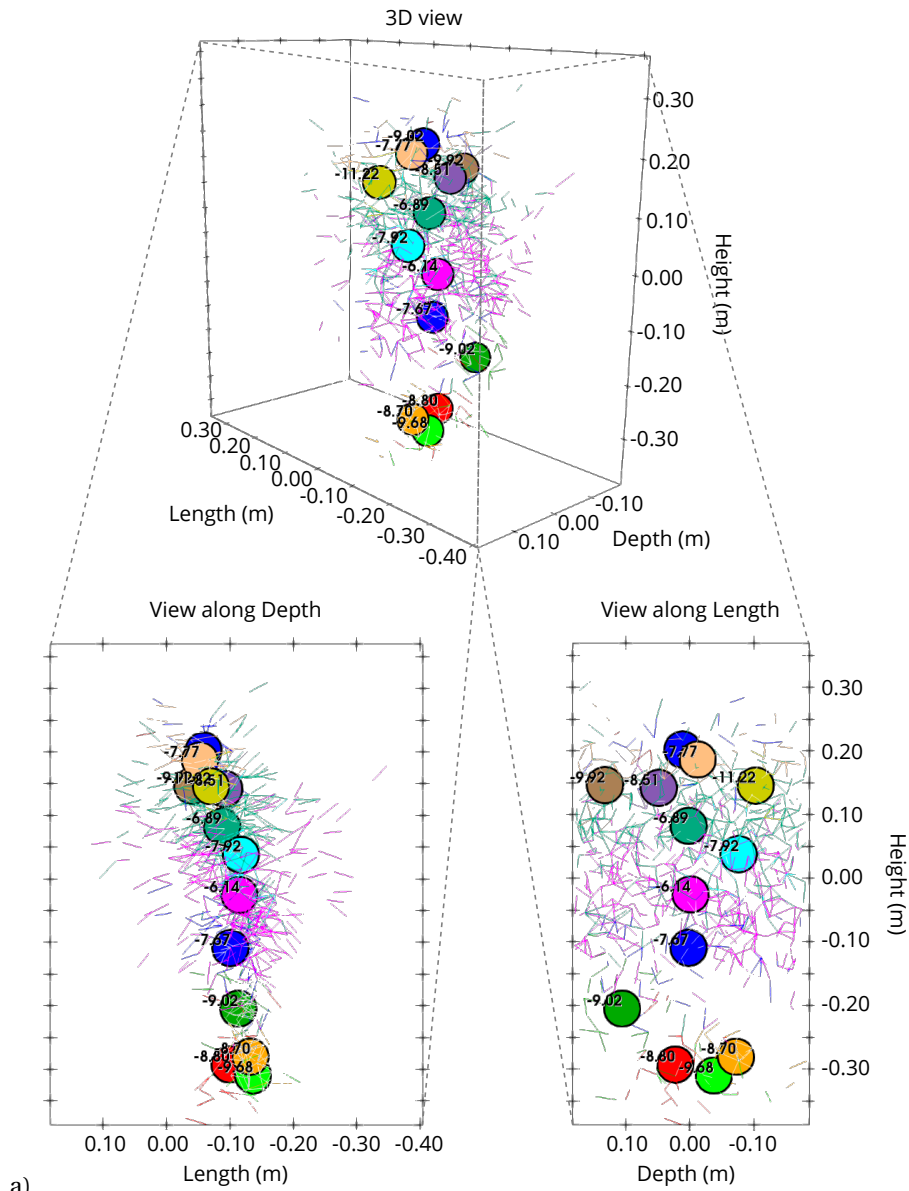
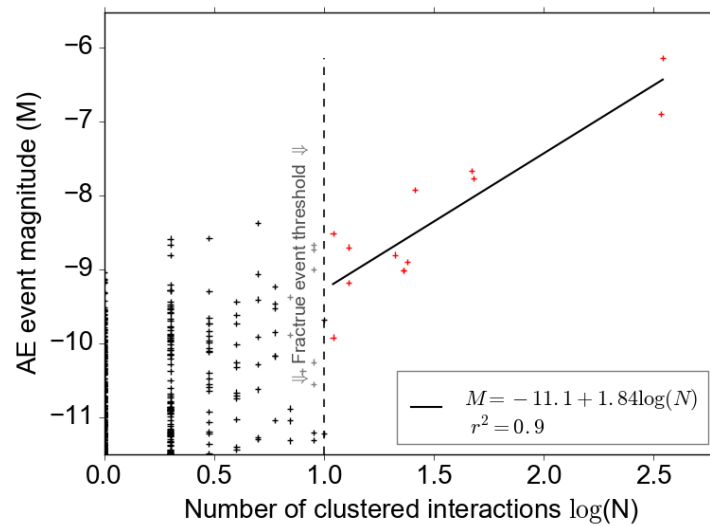


Figure 11. a) Fracture plane with respect to IPZ AE activity (95-100% max load, $\gamma=4$). Broken bonds (red), intact bonds (blue), IPZ AE events (white circles) b) Numerical model spatial AE magnitude distribution ($\gamma=4$).

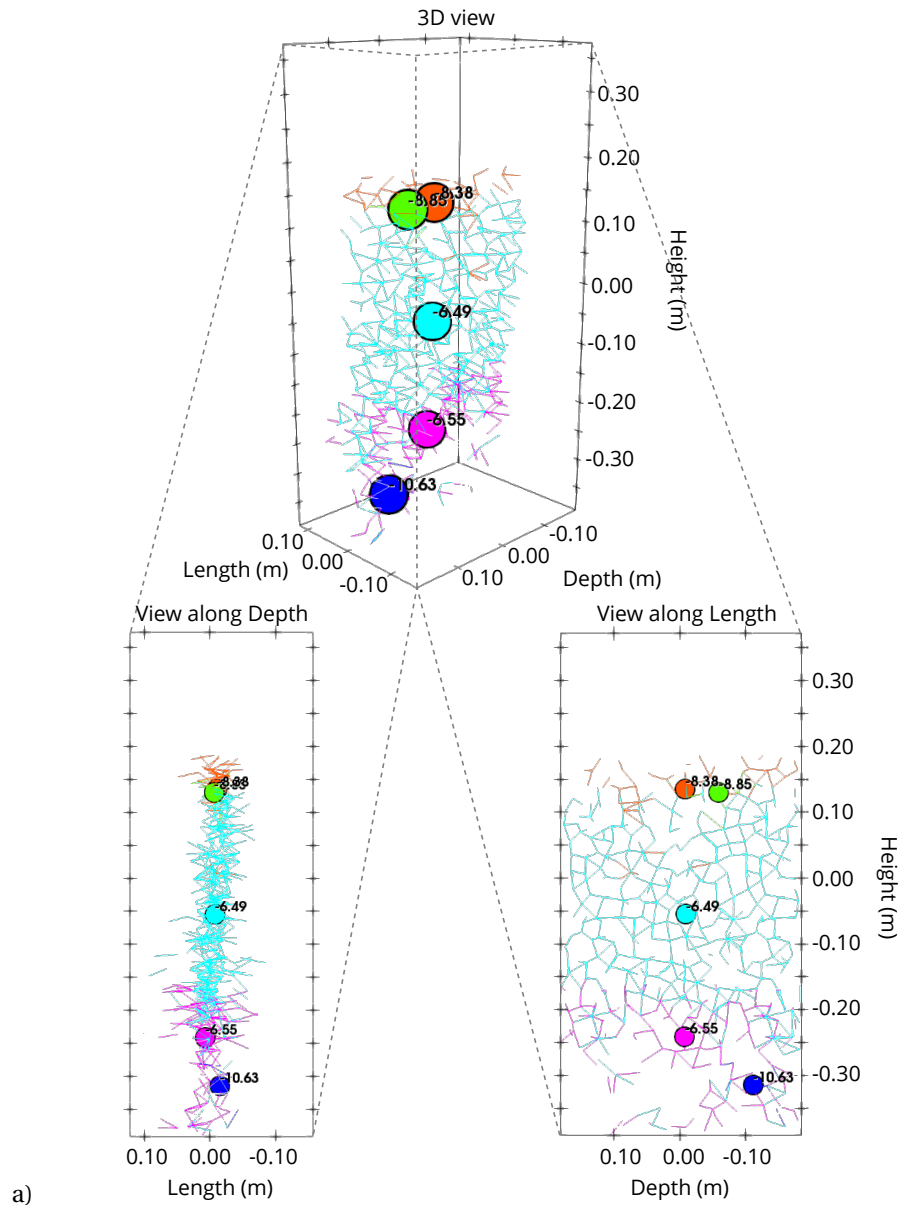


a)

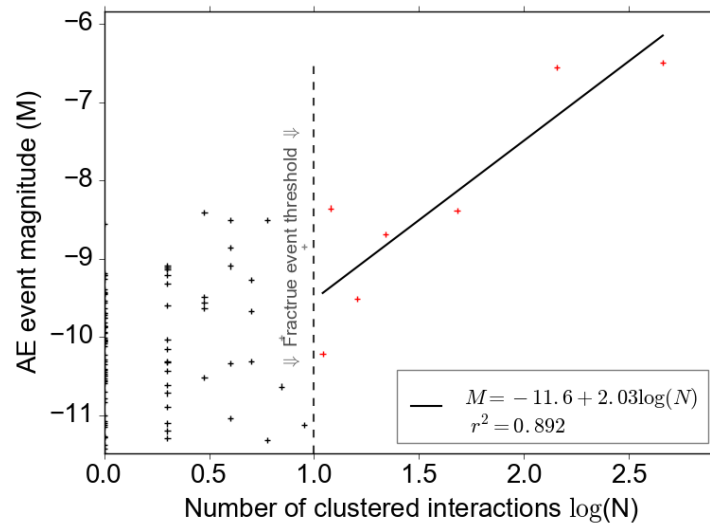


b)

Figure 12. a) Failure plane AE events (circle colors indicating event ID) comprised of ≥ 10 clustered broken bonds (line colors indicating event ID) b) Event magnitudes as a function of number of clustered interactions ($\gamma=4$)

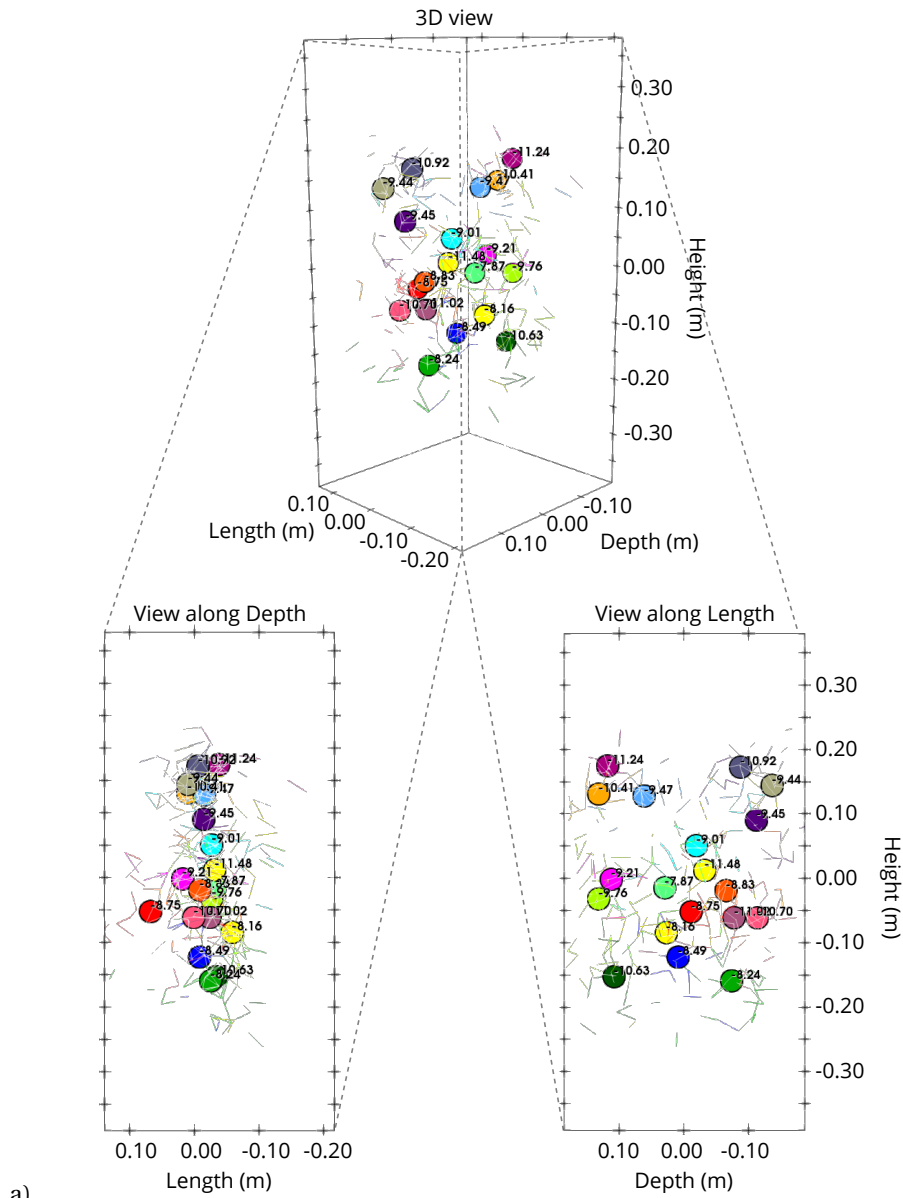


a)

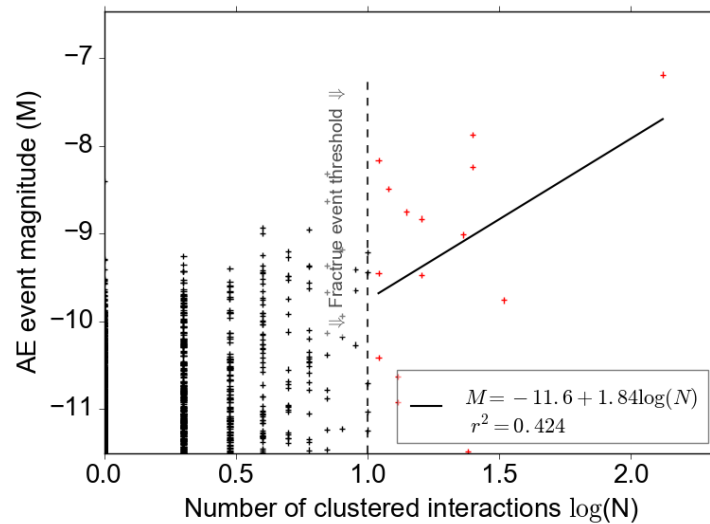


b)

Figure 13. a) Failure plane AE events (circle colors indicating event ID) comprised of ≥ 10 clustered broken bonds (line colors indicating event ID) b) Event magnitudes as a function of number of clustered interactions ($\gamma = \infty$)



a)



b)

Figure 14. a) Failure plane AE events (circle colors indicating event ID) comprised of ≥ 10 clustered broken bonds (line colors indicating event ID) b) Event magnitudes as a function of number of clustered interactions ($\gamma=2$)

5. Conclusion

The methodology presented in this paper aims to improve rock fracture modeling and relieve the computational challenge of modeling rock heterogeneities by augmenting traditional DEM with a physically constructed grain edge-interaction-length distribution (EILD). The method simulates naturally occurring heterogeneities, such as microcracks and misshapen grains, by stochastically strengthening and weakening DEM bonds according to the image analysis of rock grain interactions. The numerical Intrinsic Process Zone (IPZ) AE activity evolves similarly to IPZ observations in experimental three point bending tests. As the numerical heterogeneity increases (*i.e.*, decrease of the Weibull shape parameter, γ), the IPZ width increases. This is a clear result of the variation of bond strengths imposed by the EILD which artificially generate locally “tough” regions and stochastically distributed “microdefects” that arrest and redirect microcracks, respectively. The microcracks occur within some pre-fracture volume (sized depending on EILD variation) and ultimately coalesce to generate AE activity along the fracture. In comparison to the traditional DEM model, the EILD-augmented model is capable of using a physically constructed EILD to simulate various amounts of rock heterogeneity, while traditional DEM fails to capture the experimentally observed rock engagement prior to and following failure.

The analysis presented in this paper aims to provide deeper insight into the role of rock heterogeneities on the fracture process. Results show that larger AE events are located directly along the fracture and their magnitudes are linearly related to their number of constituent interactions. Meanwhile, smaller AE events correspond to failure of weak heterogeneities beyond the fracture. These observations lead to the development of a “fracture event threshold” to distinguish between larger fracture AE events and smaller damage AE events. Such a distinction enables the direct observation of the fracture via AE activity, even within the wider IPZ zone. Further analysis may be performed to better understand the relationship between grain scale heterogeneities and micromechanical microcrack coalescence for various rock types at different stress/strain states. This analysis may also be extended for comparison with existing continuum damage models.

In summary, this paper outlines the addition of a physically grounded source of rock heterogeneity into DEM. The value of the so-called “EILD” is demonstrated by comparing the numerically and experimentally collected pre- and post-failure AE activity during a three point bending test. After the model is validated, it is used to characterize and distinguish fracture AE activity from damage AE activity within the IPZ. Other uses for the EILD-augmented model include the validation/improvement of existing continuum damage models and understanding the relationship between grain scale heterogeneities and microcrack coalescence at various stress/strain states.

Acknowledgments

This research was in part funded by various sources including the Chateaubriand Fellowship, Laboratoire 3SR, and Ingrid Tomac at the University of California-San Diego. The author also thanks the reviewers for their valuable comments, as highlighted in the complete review history online.

References

- Ahrens, J., Geveci, B., and Law, C. (2005). ParaView: An end-user tool for large-data visualization. In *Visualization Handbook*.
- Alava, M. J., Nukala, P. K., and Zapperi, S. (2006). Statistical models of fracture. *Advances in Physics*, 55(3-4):349–476.
- Bai, Q. S., Tu, S. H., and Zhang, C. (2016). DEM investigation of the fracture mechanism of rock disc containing hole(s) and its influence on tensile strength. *Theoretical and Applied Fracture Mechanics*, 86(July):197–216.
- Berkovits, A. and Fang, D. (1995). Study of fatigue crack characteristics by acoustic emission. *Engineering Fracture Mechanics*, 51(3).
- Birck, G., Riera, J. D., and Iturrioz, I. (2018). Numerical DEM simulation of AE in plate fracture and analogy with the frequency of seismic events in SCRs. *Engineering Failure Analysis*, 93(December 2017):214–223.
- Boyce, G. M., McCabe, W. M., and Koerner, R. M. (1981). Acoustic Emission Signatures of Various Rock Types in Unconfined Compression. *Geotechnical Engineering Practice*, pages 142–154.
- Buxton, G. A., Care, C. M., and Cleaver, D. J. (2001). A lattice spring model of heterogeneous materials with plasticity. *Modelling and Simulation in Materials Science and Engineering*, 9:485–497.
- Cai, M. and Kaiser, P. (2004). Numerical simulation of the Brazilian test and the tensile strength of anisotropic rock and rocks with pre-existing cracks. *Int. J. Rock Mech. Min. Sci. & Geomech. Abstr.*, 41(3):1–6.
- Caulk, R. (2018). Stochastic augmentation of a discrete element model for the investigation of tensile rupture in heterogeneous rock. *Yade Technical Archive*.
- Chun'an Tang (1997). Numerical simulation of progressive rock failure and associated seismicity. *International journal of rock mechanics and mining sciences & geomechanics abstracts*.
- Da Cruz, F., Emam, S., Prochnow, M., Roux, J. N., and Chevoir, F. (2005). Rheophysics of dense granular materials: Discrete simulation of plane shear flows. *Physical Review E - Statistical, Nonlinear, and Soft Matter Physics*, 72(2).
- Eisenblatter, J., Grosse, C. U., Koppel, S., Kurz, J., Landis, E., Linzer, L., Manthei, G., Ohstu, M., Schechinger, B., Shigeishi, M., Shitani, T., and Vogel, T. (2008). *Acoustic Emission Testing*. Springer Berlin Heidelberg.
- Eitzen, D. and Wadley, N. (1984). Acoustic Emission : Establishing the Fundamentals. *Journal of Research of the National Bureau of Standards*, 89(1):75–100.

- Fakhimi, A., Carvalho, F., Ishida, T., and Labuz, J. (2002). Simulation of failure around a circular opening using CWFS model. *International Journal of Rock Mechanics and Mining Sciences*, 39:507–515.
- Garboczi, E. J. and Day, A. R. (1995). An algorithm for computing the effective linear elastic properties of heterogeneous materials: Three-dimensional results for composites with equal phase poisson ratios. *Journal of the Mechanics and Physics of Solids*, 43(9):1349–1362.
- Godin, N., Huguet, S., Gaertner, R., and Salmon, L. (2004). Clustering of acoustic emission signals collected during tensile tests on unidirectional glass/polyester composite using supervised and unsupervised classifiers. *NDT and E International*, 37(4):253–264.
- Hazzard, J. and Young, R. (2000). Simulating acoustic emissions in bonded-particle models of rock. *International Journal of Rock Mechanics and Mining Sciences*, 37(5):867–872.
- Hazzard, J. F. and Damjanac, B. (2013). Further investigations of microseismicity in bonded particle models. *3rd International FLAC/DEM Symposium*, pages 1–11.
- Hazzard, J. F. and Young, R. P. (2002). Moment tensors and micromechanical models. *Tectonophysics*, 356:181–197.
- Hazzard, J. F. and Young, R. P. (2004). Dynamic modelling of induced seismicity. *International Journal of Rock Mechanics and Mining Sciences*, 41(8):1365–1376.
- Houseknecht, D. (1991). Use of cathodoluminescence petrography for understanding compaction, quartz cementation, and porosity in sandstones. *Luminescence Microscopy: Quantitative and Qualitative Aspects*, pages 59–66.
- Itasca, C. (2015). Pfc-particle flow code in 2 and 3 dimension.
- Iturrioz, I., Birck, G., and Riera, J. D. (2019). Numerical DEM simulation of the evolution of damage and AE preceding failure of structural components. *Engineering Fracture Mechanics*, 210(2018):247–256.
- Khazaei, C., Hazzard, J., and Chalaturnyk, R. (2015). Damage quantification of intact rocks using acoustic emission energies recorded during uniaxial compression test and discrete element modeling. *Computers and Geotechnics*, 67(2015):94–102.
- Khazaei, C., Hazzard, J., and Chalaturnyk, R. (2016). A discrete element model to link the microseismic energies recorded in caprock to geomechanics. *Acta Geotechnica*, 11(6):1351–1367.
- Labuz, J. F. and Biolzi, L. (2007). Experiments with rock: Remarks on strength and stability issues. *International Journal of Rock Mechanics and Mining Sciences*, 44(4):525–537.
- Labuz, J. F., Cattaneo, S., and Chen, L. H. (2001). Acoustic emission at failure in quasi-brittle materials. *Construction and Building Materials*, 15(5-6):225–233.
- Labuz, J. F., Shah, S. P., and Dowding, C. H. (1987). The fracture process zone in granite: evidence and effect. *International Journal of Rock Mechanics and Mining Sciences and*, 24(4):235–246.
- Lei, X., Masuda, K., Nishizawa, O., Jouniaux, L., Liu, L., Ma, W., Satoh, T., and Kusunose, K. (2004). Detailed analysis of acoustic emission activity during catastrophic fracture of faults in rock. *Journal of Structural Geology*, 26:247–258.
- Lei, X.-L., Kusunose, K., Nishizawa, O., Cho, A., and Satoh, T. (2000). On the spatio-temporal distribution of acoustic emissions in two granitic rocks under triaxial compression: The role of pre-existing cracks. *Geophysical Research Letters*, 27(13):1997–2000.
- Li, B. Q. and Einstein, H. H. (2017). Comparison of Visual and Acoustic Emission Observations in a Four Point Bending Experiment on Barre Granite. *Rock Mechanics and Rock Engineering*, 50(9):2277–2296.
- Lisjak, A., Liu, Q., Zhao, Q., Mahabadi, O. K., and Grasselli, G. (2013). Numerical simulation of acoustic emission in brittle rocks by two-dimensional finite-discrete element analysis. *Geophysical Journal International*, 195(1):423–443.
- Liu, H. Y., Roquete, M., Kou, S. Q., and Lindqvist, P. A. (2004). Characterization of rock heterogeneity and numerical verification. *Engineering Geology*, 72(1-2):89–119.
- Lockner, D. A. (1993). The role of acoustic emission in the study of rock fracture. *International Journal of Rock Mechanics and Mining Sciences & Geomechanics Abstracts*, 30(7):883–899.
- Lockner, D. A., Byerlee, J. D., Kuksenko, V., Ponomarev, A., and Sidorin, A. (1992). Chapter 1 Observations of Quasistatic Fault Growth from Acoustic Emissions. *International Geophysics*, 51(C):3–31.
- Ma, Y. and Huang, H. (2017). Tensile strength calibration in DEM modeling. *American Rock Mechanics Association*.
- Mahabadi, O., Grasselli, G., and Munjiza, A. (2009). Numerical modelling of a Brazilian Disc test using the combined finite-discrete element method. In Diederichs, M. and Grasselli, G., editors, *CANUS Rock Mechanics Symposium*, Toronto.
- McLaskey, G. C., Lockner, D. A., Kilgore, B. D., and Beeler, N. M. (2015). A robust calibration technique for acoustic emission systems based on momentum transfer from a ball drop. *Bulletin of the Seismological Society of America*, 105(1):257–271.
- Meng, Q., Zhang, M., Han, L., Pu, H., and Nie, T. (2016). Effects of Acoustic Emission and Energy Evolution of Rock Specimens Under the Uniaxial Cyclic Loading and Unloading Compression. *Rock Mechanics and Rock Engineering*, 49(10):3873–3886.
- Nitka, M. and Tejchman, J. (2016). Mesoscopic Simulations of Concrete Fracture Based on X-ray CT Images of Interior Structure. In *9th International Conference on Fracture Mechanics of Concrete and Concrete Structures*.
- Ostoja-Starzewski, M., Sheng, P. Y., and Jasiuk, I. (1994). Influence of random geometry on effective properties and damage formation in composite materials. *J. Eng. Mat. Tech.*, 116(July 1994):384–391.
- Potyondy, D. O. and Cundall, P. A. (2004). A bonded-particle model for rock. *International Journal of Rock Mechanics and Mining Sciences*, 41(8):1329–1364.
- Rabczuk, T. and Eibl, J. (2006). Modelling dynamic failure of concrete with meshfree methods. *International Journal of Impact Engineering*, 32(11):1878–1897.

- Rao, M. V. M. S. and Lakshmi, K. J. P. (2005). Analysis of b-value and improved b-value of acoustic emissions accompanying rock fracture. *Current Science*, 89(9):1577–1582.
- Rasband, W. (2012). ImageJ. U. S. National Institutes of Health, Bethesda, Maryland, USA, page imagej.nih.gov/ij.
- Rodríguez, P., Arab, P. B., and Celestino, T. B. (2016). Characterization of rock cracking patterns in diametral compression tests by acoustic emission and petrographic analysis. *International Journal of Rock Mechanics and Mining Sciences*, 83:73–85.
- Saksala, T. (2015). Rate-Dependent Embedded Discontinuity Approach Incorporating Heterogeneity for Numerical Modeling of Rock Fracture. *Rock Mechanics and Rock Engineering*, 48(4):1605–1622.
- Scholtès, L. and Donzé, F. V. (2012a). A DEM model for soft and hard rocks: Role of grain interlocking on strength. *Journal of the Mechanics and Physics of Solids*, 61:352–369.
- Scholtès, L. and Donzé, F.-V. (2012b). Modelling progressive failure in fractured rock masses using a 3D discrete element method. *International Journal of Rock Mechanics and Mining Sciences*, 52:18–30.
- Scholz, C. H. (1968). The frequency-magnitude relation of microfracturing in rock and its relation to earthquakes. *Seismological Society of America*, 58(1):399–415.
- Scholz, C. H. and Harris, R. A. (2003). "The Mechanics of Earthquakes and Faulting - Second Edition" by Christopher H. Scholz. *Seismological Research Letters*, 74(3):333–333.
- Sfantos, G. K. and Aliabadi, M. H. (2007). Multi-scale boundary element modelling of material degradation and fracture. *Computer Methods in Applied Mechanics and Engineering*, 196(7):1310–1329.
- Shah, K. R. and Labuz, J. F. (1995). Damage mechanism in stressed rock from acoustic emission. *Journal of Geophysical Research*, 100:15527–15539.
- Shearer, P. (2009). *Introduction to Seismology*. Cambridge University Press.
- Smilauer, V., Catalano, E., Chareyre, B., Dorofeenko, S., Duriez, J., Dyck, N., Elias, J., Er, B., Eulitz, A., Gladky, A., Guo, N., Jakob, C., Kneib, F., Kozicki, J., Marzougui, D., Maurin, R., Modenese, C., Scholtes, L., Sibille, L., Stran-sky, J., Sweijen, T., Thoeni, K., and Yuan, C. (2015). *Yade Documentation 2nd ed.* Zenodo.
- Soma, N., Niitsuma, H., and Baria, R. (2002). Reflection technique in time-frequency domain using multicomponent acoustic emission signals and application to geothermal reservoirs. *Geophysics*, 67(3):928–938.
- Sondergeld, C. H. and Estey, L. H. (1981). Acoustic emission study of microfracturing during the cyclic loading of Westerly granite. *Journal of Geophysical Research*, 86(B4):2915–2924.
- Tan, Y., Yang, D., and Sheng, Y. (2009). Discrete element method (DEM) modeling of fracture and damage in the machining process of polycrystalline SiC. *Journal of the European Ceramic Society*, 29(6):1029–1037.
- Tang, C. and Kaiser, P. (1998). Numerical Simulation of Cumulative Damage and Seismic Energy Release During Brittle Rock Failure—Part I: Fundamentals. *International Journal of Rock Mechanics and Mining Sciences*, 35(2):113–121.
- Wang, S. Y., Sloan, S. W., Sheng, D. C., and Tang, C. A. (2012). Numerical analysis of the failure process around a circular opening in rock. *Computers and Geotechnics*, 39(2012):8–16.
- Wang, X. L. and Li, J. C. (2014). Simulation of triaxial response of granular materials by modified DEM. *Science China: Physics, Mechanics and Astronomy*, 57(12):2297–2308.
- Yang, S. Q., Jing, H. W., and Wang, S. Y. (2012). Experimental investigation on the strength, deformability, failure behavior and acoustic emission locations of red sandstone under triaxial compression. *Rock Mechanics and Rock Engineering*, 45(4):583–606.
- Yang, T. H., Tham, L. G., Tang, C. A., Liang, Z. Z., and Tsui, Y. (2004). Influence of heterogeneity of mechanical properties on hydraulic fracturing in permeable rocks. *Rock Mechanics and Rock Engineering*, 37(4):251–275.
- Zang, A., Wagner, F. C., Stanchits, S., Dresen, G., Andersen, R., and M.Haidekker (1998). Source analysis of acoustic emission in Aue granite cores under symmetric and asymmetric loads. *Geophysical Journal International*, 135:1113.
- Zhang, X.-P., Zhang, Q., and Wu, S. (2017). Acoustic emission characteristics of the rock-like material containing a single flaw under different compressive loading rates. *Computers and Geotechnics*, 83(2017):83–97.
- Zietlow, W. K. and Labuz, J. F. (1998). Measurement of the Intrinsic Process Zone in rock using acoustic emission. *Int. J. Rock Mech. Min. Sci.*, 35(3):291–299.

6. Appendices

6.1. Newton Raphson maximum-likelihood parameter estimation for EILD:

The Weibull distribution is an exponential probability density function (PDF) described by a shape parameter (γ) and scale parameter (θ):

$$\phi = f(x_i|\theta, \gamma) = \left(\frac{\gamma}{\theta}\right)\left(\frac{x}{\theta}\right)^{\gamma-1} \exp(-(x/\theta)^\gamma) \quad (21)$$

We use the log-likelihood of the PDF for a maximum likelihood parameter estimation:

$$L(\theta, \gamma) = \sum_{i=1}^n \ln f(x_i|\theta, \gamma) \quad (22)$$

all summations from here on are w.r.t x_i from $i = 1$ to n

$$\ln L = n \ln \gamma - n \ln \theta - \sum \left(\frac{x}{\theta}\right)^\gamma + (\gamma - 1) \sum \ln x \quad (23)$$

$$\frac{d \ln L}{d \gamma} = \frac{n}{\gamma} - n \ln \theta - \sum \left(\frac{x}{\theta}\right)^\gamma \ln \frac{x}{\theta} + \sum \ln x = 0 \quad (24)$$

$$\frac{d \ln L}{d \theta} = -\frac{n \gamma}{\theta} + \sum \frac{\gamma \left(\frac{x}{\theta}\right)^\gamma}{\theta} = 0 \quad (25)$$

now we solve for θ

$$\theta = \left(\frac{\sum x^\gamma}{n}\right)^{\frac{1}{\gamma}} \quad (26)$$

and plug into $\frac{d \ln L}{d \gamma}$

$$f(\gamma) = \frac{\sum x^\gamma \ln x}{\sum x^\gamma} - \frac{\sum \ln x}{n} - \frac{1}{\gamma} \quad (27)$$

and the derivative for Newton-Raphson:

$$\frac{d f}{d \gamma} = \frac{\sum x^\gamma \ln^2 x - (\sum x^\gamma \ln x)^2}{(\sum x^\gamma)^2} + \frac{1}{\gamma^2} \quad (28)$$

where γ is solved for iteratively with Newton-Raphson:

$$\gamma = \gamma_o + \frac{f(\gamma)}{\frac{d f}{d \gamma}} \quad (29)$$

once γ is obtained, it is used to obtain θ

6.2. Comparison of numerical and experimental elastic waves

In an effort to increase confidence in the AE scheme, the present study compares the propagation of numerical elastic waves caused by AE in the DEM specimen to the propagation of elastic waves in experimental specimens. To do so, numerical “transducers” (Fig. 6) are used to monitor displacements caused by the release of energy during an AE event. Following the same methodology used in experiments [Eisenblatter et al., 2008], the arrival time residuals are minimized with least squares to estimate an AE event origin. Numerical transducer waveforms look like Fig. 15a with a manually picked arrival time for each waveform as shown in Fig. 15b. After the arrival times are picked for an

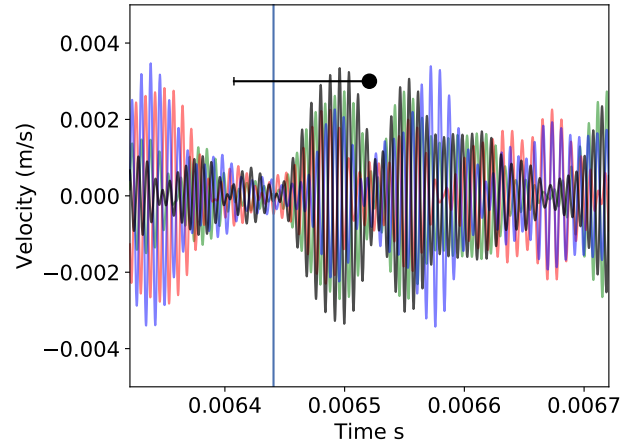


Figure 15. An example AE event numerical waveform showing manual arrival time selection (vertical line) and micromechanical event duration (black line)

event, the residuals are minimized using least squares:

$$t_i = \frac{\sqrt{(x-x_i)^2 + (y-y_i)^2 + (z-z_i)^2}}{v} + t_o \quad (30)$$

$$r_i = \left(\frac{\partial t}{\partial x_i} \Delta x\right) + \left(\frac{\partial t}{\partial y_i} \Delta y\right) + \left(\frac{\partial t}{\partial z_i} \Delta z\right) + \Delta t \quad (31)$$

$$r = \mathbf{G} \Delta m \quad (32)$$

where t_i is the manually selected arrival time for each of the transducers, i , v is the P-Wave velocity of the medium, x , y , z are coordinates for an initial guess of the unknown origin of the event, x_i , y_i , z_i are the coordinates of transducer i , \mathbf{G} is the matrix containing the partial derivatives of Eq. 30 and \mathbf{r} is the vector of residuals.

As shown in Fig. 16 the estimated AE event origin compares well to the true micromechanical AE event location. Therefore the elastic waves generated by the release of strain energy in the numerical specimen are behaving in a similar manner to those observed in an experimental setting.

Manuscript received 16th August 2019, accepted 14th April 2020.

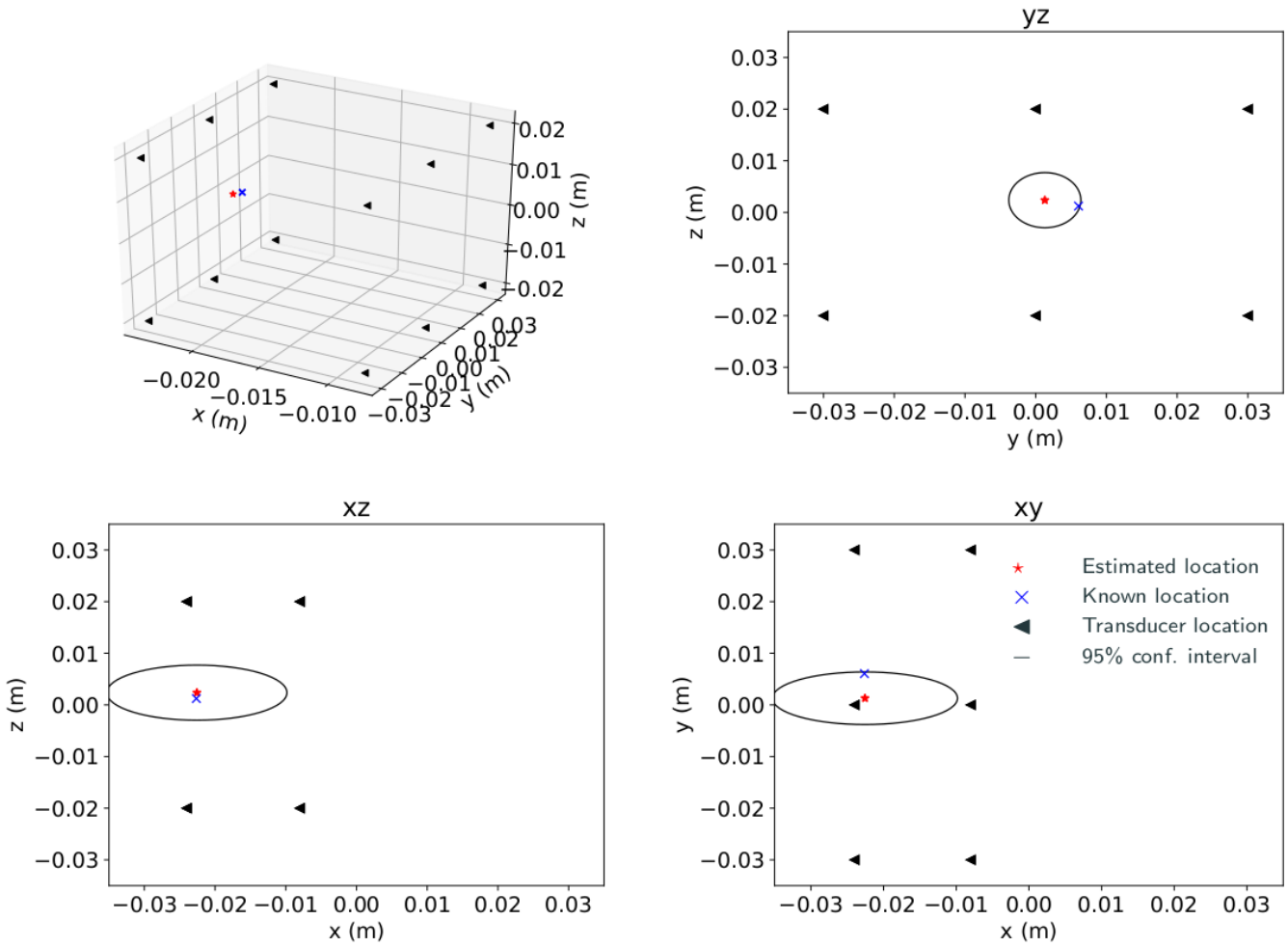


Figure 16. Predicted (red star) and micromechanical origin (blue x) of acoustic emission event.